Acoustic emission source location using Lamb wave propagation simulation and artificial neural network for I-shaped steel girder

Cheng, Lu; Xin, Haohui; Groves, Roger M.; Veljkovic, Milan

DOI
10.1016/j.conbuildmat.2020.121706

Publication date
2021

Document Version
Final published version

Published in
Construction and Building Materials

Construction and Building Materials 273 (2021) 121706

Contents lists available at ScienceDirect

Construction and Building Materials

journal homepage: www.elsevier.com/locate/conbuildmat

Acoustic emission source location using Lamb wave propagation simulation and artificial neural network for I-shaped steel girder

Lu Cheng [a], Haohui Xin [b,a], Roger M. Groves [c], Milan Veljkovic [a]

[a] Steel and Composite Structures Group, Faculty of Civil Engineering and Geosciences, Delft University of Technology, The Netherlands
[b] Department of Civil Engineering, School of Human Settlements and Civil Engineering, Xi'an Jiaotong University, Xi'an, China.
[c] Aerospace Non-Destructive Testing Laboratory, Faculty of Aerospace Engineering, Delft University of Technology, The Netherlands

HIGHLIGHTS

- Acoustic emission (AE) for structural health monitoring (SHM)
- Artificial neural networks (ANN) based source localization methods.
- Trained neural networks sucussfully predicted the AE source location.

ARTICLE INFO

Article history:
Received 4 May 2020
Received in revised form 29 October 2020
Accepted 12 November 2020
Available online 4 December 2020

Keywords:
Source location
Lamb waves
Time of arrival (TOA)
Finite element analysis
Artificial neural network (ANN)
Composite structures

ABSTRACT

Acoustic emission (AE) is often used for structural health monitoring (SHM) in the wide field of engineering structures and one of its most beneficial attributes is the ability to localize the damage/crack based on the AE events. The vast majority of ongoing work on AE monitoring focues on geometrically simple structures or a confined area, but the AE source location strategies are rather complicated for real engineering structures. In this paper, an effective method for source localization in realistic structures is presented based on the application of artificial neural networks (ANN), using finite element (FE) simulation results of Lamb waves as the modelling basis. Pencil lead break experiments and related FE simulations on a steel-concrete composite girder are conducted to evaluate the performance of the method. The identification of different wave modes is carried by comparing alternative onset time detection methods. Numerical results are found to be matching closely with the experimental results. To get a reliable ANN model, the validated FE model is used to create a comprehensive database with five different sensor arrangements. It is found that the proposed method is superior to the classical Time of Arrival (TOA) method with the same input data. The results indicate that using trained neural networks based on numerical data is a viable option for AE source location in the case of the I-shaped girder, increasing the likelihood of design and optimization of the AE technique in monitoring realistic structures.

1. Introduction

Many in-service structures suffer the problems of cumulative damages resulting from overloading and fatigue cracks with increased age [1]. In order to assess the service life of existing structures and reduce maintenance costs, a need for a reliable and rigorous monitoring system for engineering structures is evident. Acoustic Emission (AE) is a non-destructive testing (NDT) technique which uses acoustic wave generated by a rapid release of energy within a material for structural health monitoring (SHM) [2]. The use of the AE technique provides the potential for early damage detection and real-time monitoring of the structures [3,4]. One of the most essential features of the AE technique is the ability to localize the damage/crack based on the AE events. Identifying the source location can allow an accurate global investigation of a structure and a prior understanding of the specific possible damaged/cracked area [5]. It can also lead to a better insight into the nature of the source mechanism, as certain AE sources are only related to a particular load case and geometric characteristics [6]. For example, AE source location methods can contribute to effectively eliminate AE signals emitted from unwanted AE sources. The source mechanism under a certain load regime can then be defined more accurately.

AE source location determination can be one, two, or three dimensional according to the structure of interest. Many structures can be simplified to a plate-like structure since most practical

E-mail address: H.Xin@tudelft.nl (H. Xin)

https://doi.org/10.1016/j.conbuildmat.2020.121706
0950-0618/

structures have one dimension that is considerably smaller than the other two dimensions. Simple plate wave theory was proposed and applied to explain AE wave propagation in plate-like structures. Several researchers demonstrated that Lamb waves are the dominant mode of disturbance propagation in plate-like structures [7,8]. In addition, Lamb waves show great potential for structural health monitoring (SHM) due to their capability of long propagation distance, low attenuation, and high sensitivity to small imperfections [9,10]. Rose [11] summarized the potential damage types that a Lamb-wave based detection method can provide. A Lamb-wave based detection method can supply relevant information for estimation of structural behaviour [12–14], confirmation of the presence of the damage [15,16], determination of the location of damage [17], assessment of the size of damage [18,19], and prediction of the remaining service life [20–22].

The standard method for two-dimensional source location, known as the time of arrival (TOA) method [23], is discussed in detail in the NDT handbook [24]. It has been widely used to locate AE source in isotropic structures based on the detected arrival time of signals at given sensors. The established TOA method relies on the assumption of isotropic wave velocity in all directions and an uninterrupted propagation path. This is certainly not the case in realistic structures where geometric features such as holes, irregular boundaries, and other structural discontinuities will significantly interrupt the propagation path and velocity [25,26]. Besides, the propagation distance, source amplitude, and wave dispersion behaviour make it difficult to determine the wave arrival time with precision. Any errors in the determination of signal arrival time will result in a further loss of accuracy in the estimated source locations. Except for the factors discussed above, the detection system also has an impact on localization accuracy. As the exact damage positions could not be known until the impact happens, a standardized number and arrangement of sensors are not available for all types of realistic structures [27]. Hence, an approach for AE source location which can be applied to realistic structures is still challenging. Several research papers have reported strategies to improve the AE source location accuracy for simple geometry structures in the laboratory level, including the wave velocity-based method [28,29], the none wave velocity-based method [30–32], the statistical method [33,34], and the mapping method [35,36].

Artificial intelligent techniques have also been researched and applied in SHM of complex systems, such as ANN [37,38], Random Forest Regressor [39], and Generalized Regression [40]. Specifically, a well-trained ANN could be used to predict outcomes without a good knowledge of explicit analytical functions. During the training of the network, the characteristics inherent to the system can be reproduced by a symbolic function relation established between the input data and output data. Hence, ANN is very promising to solve the above mentioned AE source location problems. The application of the artificial neural network (ANN) to AE source location has been demonstrated to compensate for the effects of acoustic anisotropy, boundary reflections, and obstacles in the propagation path [41,42] due to its ability to handle complex problems [43]. The practicality of combining ANN with the AE technique for global monitoring of realistic structures is worth investigating. However, due to limitations such as the lack of physical interpretation and standardized neural networks, the use of ANN for SHM of realistic composite structures has not been fully exploited. The training of the neural network is, to a large extent, related to the configuration of the monitoring system, and the geometric and physical features of the target structures. A vast majority of the experimental database of AE testing is required to interpret the signals in the right way and establish a well-trained ANN neutral network for AE source location. Obtaining such database through experiments is labour-intensive, time and economic consuming.

In order to minimize the required experiments, an alternative way is using finite element (FE) simulation to investigate the underlying mechanism of AE detection [8,44]. Most of the existing studies using the FE model for wave propagation simulation are focused on flat plates and simple geometry. Referring to realistic structures, FE analysis is mainly used to identify regions of possible damage locations which can then be regarded as primary areas of concern for structural monitoring [5]. To the best of the authors' knowledge, research in using FE analysis to simulate wave propagation within a realistic structure is rather limited [45]. Thus, as shown in Fig. 1, a surrogate method for the source location of realistic structures is proposed in this paper by combing ANN with FE analysis after experimental verification.

In this paper, acoustic emission source localization using Lamb wave propagation simulation and ANN is performed on a steel-concrete composite girder. Laboratory experiments are presented to extract test signals at distinct positions using pencil break excitation (Hsu-Nielsen source). Numerical modelling is conducted to simulate Lamb wave propagation in the tested girder. After validation of the finite element model, modal analysis is performed with a variety of onset time detection methods to identify different wave modes from experimental and numerical results. The localization results of the trained neural network are compared to the classical localization method.

2. Experimental investigation

In order to evaluate the performance of the proposed ANN-based technique against the classical TOA method, an experiment using the AE technique for predicting pencil break excitation (PBE) positions is conducted. The experiment is undertaken on an I-girder (IPE 400), which is a part of a composite steel–concrete girder from a real car park building, as shown in Fig. 2. The simply-

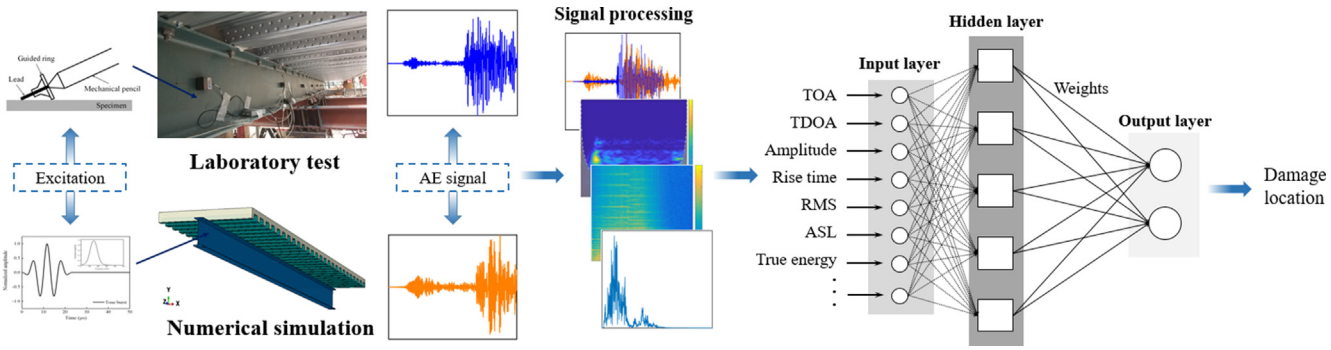

Fig. 1. The architecture of ANN structure for damage identification.

supported 8.3 m long composite steel–concrete girder (Fig. 3) consists of an IPE400 steel beam (h = 400 mm × b = 180 mm × t_w = 8.6-mm) and 150 mm thick concrete slab with ComFlor95 profiled sheeting. Although the wave propagation in the composite steel–concrete girder will be considerably influenced by structural discontinuities and composite materials, they are not considered in this study, which instead focuses upon the wave propagation within the steel beam. The damages in the steel beam, including fatigue, corrosion, and structural deterioration, are likely to occur due to the heavy vehicle loads and chemical attack [46]. The application of the AE technique on the composite girder is interesting to perform in laboratory conditions to calibrate the response of in-situ monitoring. During the experiment, it is assumed that the specimen is free of any pre-stress conditions; hence, any changes in the characteristics of the wave propagation in the steel beam are consequently correlated with the Lamb wave excitation.

The classical Hsu-Nielsen source (pencil break excitation) is used to generate crack-like AE signals on the surface of the steel beam web [47]. For detecting AE signals, seven AE sensors of 150 kHz resonance frequency (R15α, PAC) are mounted on the sur-

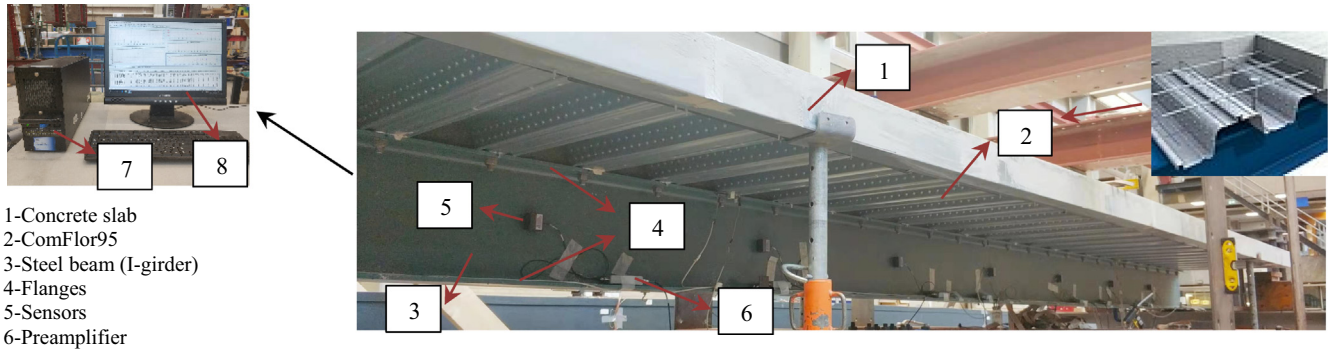

Fig. 2. Laboratory AE test of composite girder configuration.

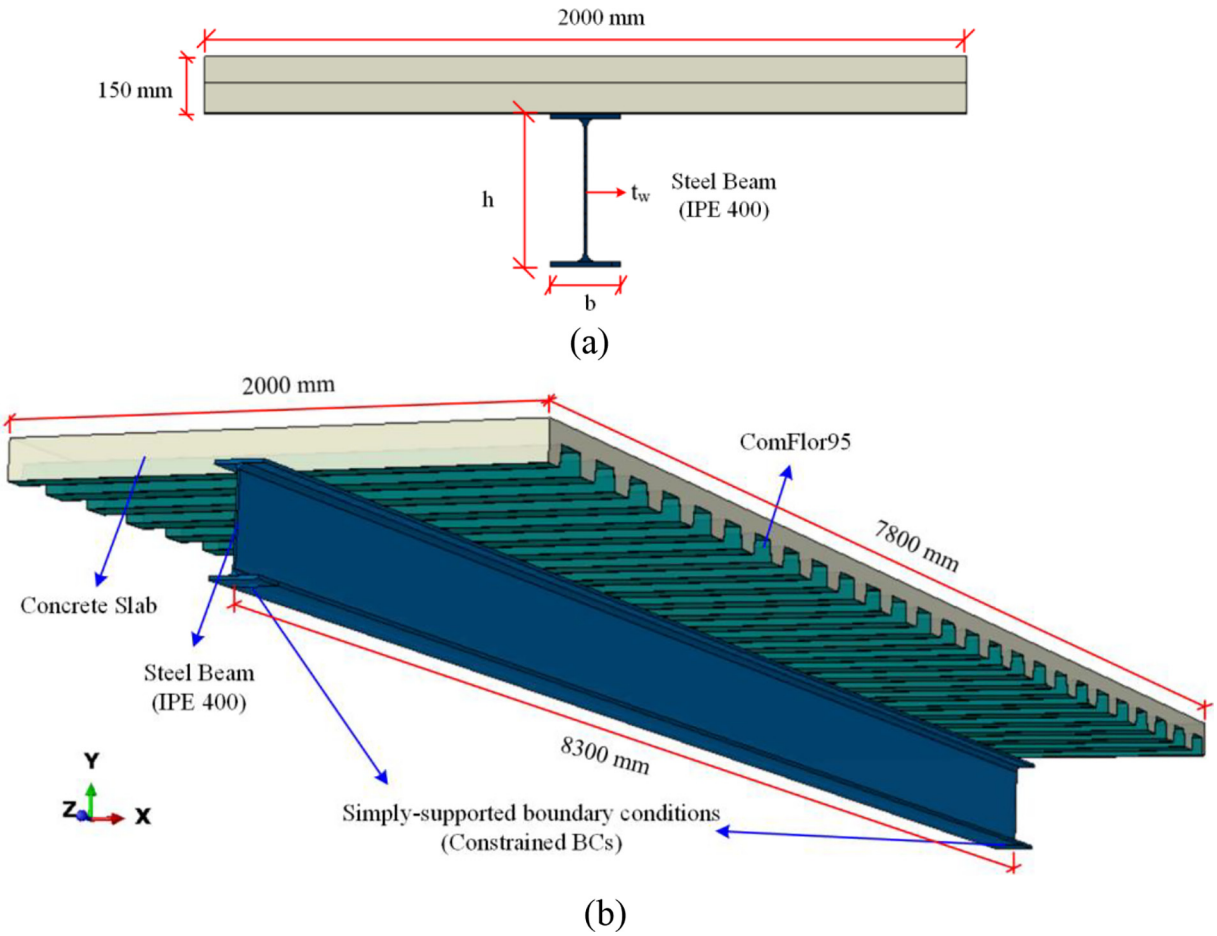

Fig. 3. Dimension of the composite steel–concrete girder (a) Cross-section view and (b) Three-dimensional view.

face of the beam web. The AE sensor and its frequency sensitivity spectrum are shown in Fig. 4. All signals are detected using an Express-8, PAC acquisition system with 40 dB pre-amplification, 42 dB threshold level, and 10 MSPS sampling rate (one sample per 0.1 μs). To provide a suitable acoustic transmission, silicone grease is used as a couplant. A Band Pass Filter of 20–400 kHz is set in the AEwin acquisition software control, as the most signals are expected in that range. The exact positions of the signals source and sensors are denoted as "E" and "s" respectively. The sequence and arrangement of exciters and sensors are distinguished by a number. Each pencil break excitation (PBE) is repeated 3 times at the same location on the beam. To assure the accuracy of the tests, almost equal lengths of pencil leads (4.0 mm) are broken with the same angle to the surface of the beam (Fig. 5(c)). Two types of sensor layout are designed as shown in Fig. 5, namely the linear layout of seven sensors (Fig. 5(a)) and the rectangular array of four sensors (Fig. 5(b)). The aim of the linear array is to get the wave velocity for the source location in the rectangular array. As shown in Fig. 5, sensors are placed as far away from each other as possible in order to maximize the sensor coverage area, which spanned 6 m. The velocity anisotropy caused by propagation distance and interrupted propagation path could be the main challenge for AE source location in the steel beam.

According to the test results of the linear array (Fig. 5(a)), the average wave propagation velocity is determined as 5219 m/s based on the time difference and the distance between sensors (1 m). Fig. 6 shows a typical example of the PBE signals generated at E1 and captured by sensors s1 and s2 of Fig. 5(a). The arrival time obtained from the AEwin system ($t_{TOA,s1}$ and $t_{TOA,s2}$) is defined when the signal amplitude is firstly larger than the user-defined threshold 42 dB (0.0125 v), as detailed in the scale-up view (Fig. 6). After that, the TOA method [48] is applied to identify its feasibility in the source localization of rectangular array (Fig. 5 (b)). The procedures of this method are described briefly below: a) Construct a grid on the interesting area within which AE events will be located. Each node position within the grid is regarded as a

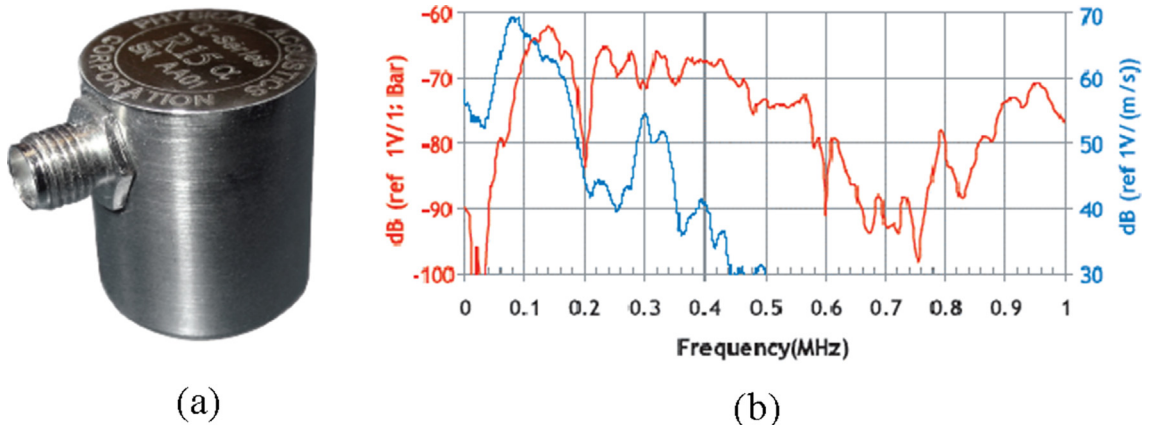

Fig. 4. (a) R15α AE sensor; (b) Frequency sensitivity spectrum of the R15α AE sensor.

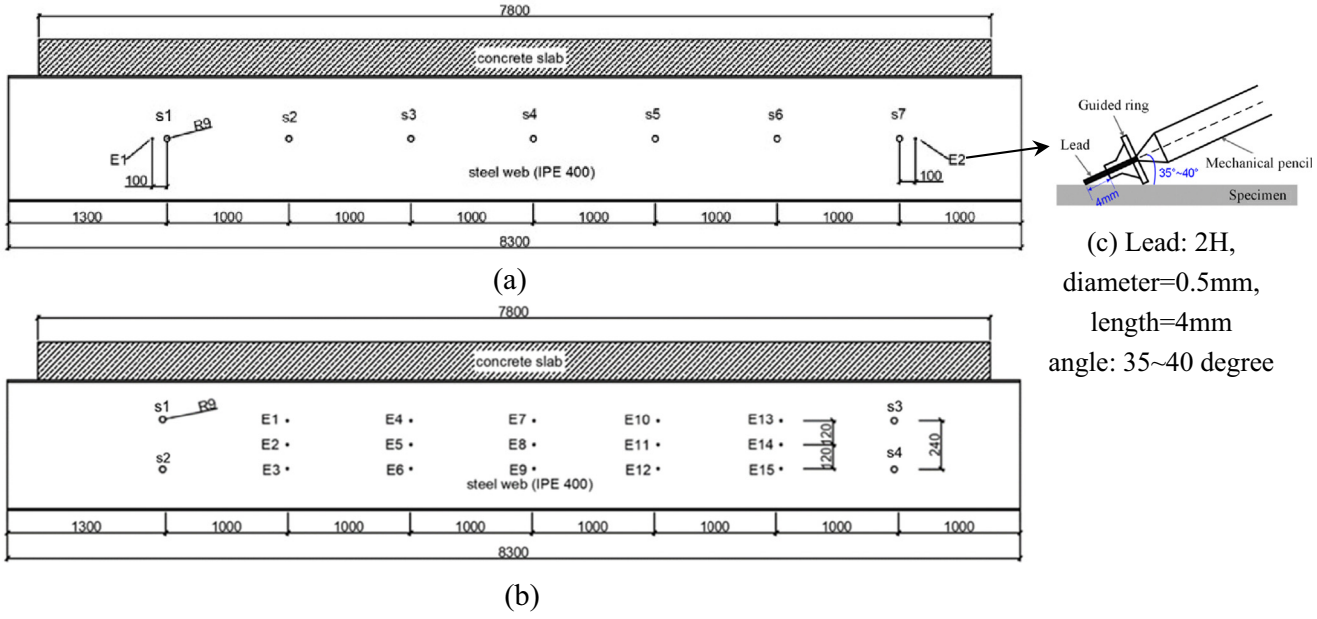

Fig. 5. Measurement setup including source location and sensor layout: Schematic view (a) Linear array (seven sensors); (b) Rectangular array (four sensors) and (c) Standard pencil leads breaking.

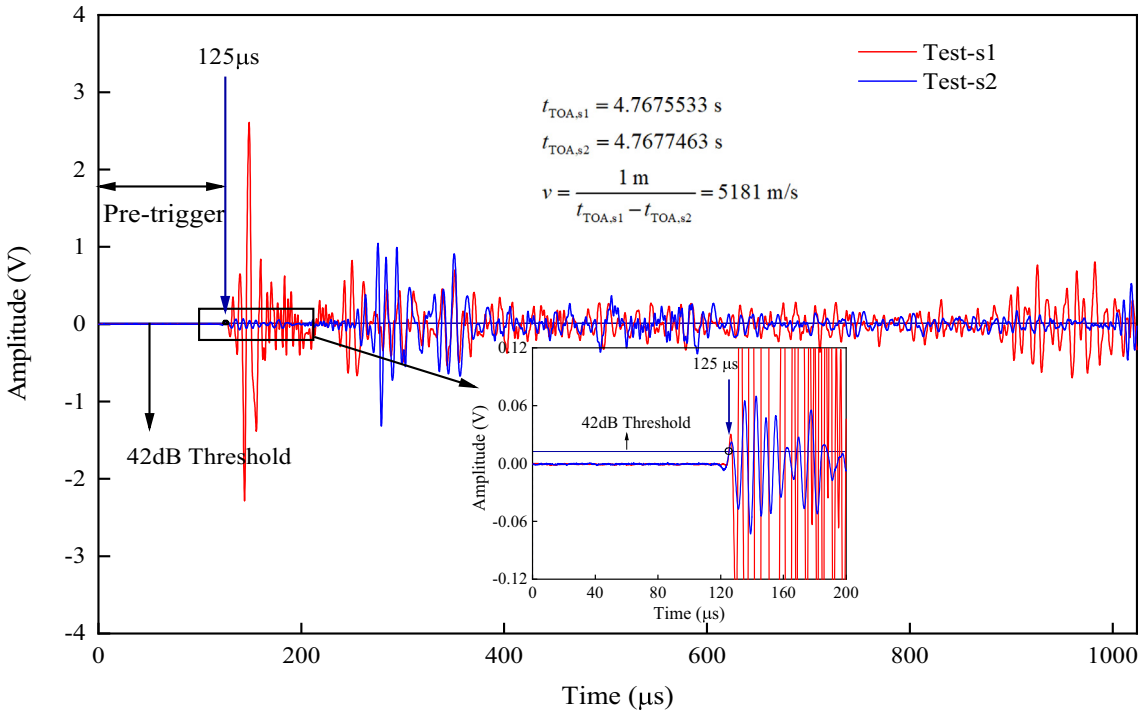

Fig. 6. Response signal and threshold line at 42 dB at sensor 1 (red) and sensor 2 (blue), obtained from the PBE exerted at E1 in Fig. 5(a). (For interpretation of the references to color in this figure legend, the reader is referred to the web version of this article.)

"guessed" location; b) the arrival time from any point in the grid to each sensor is computed from the hypothetical positions and a user-defined velocity model. It is suggested that the grid can be made as fine as computationally possible; c) comparison of the measured ($\Delta t_{i,\text{mea}}$) and calculated ($\Delta t_{i,\text{calc}}$) arrival time difference is used to determine the point of best agreement, which involves the lowest value of the objective function χ as expressed in Eqs. (1)–(3) [48]:

$$\chi = \sum \left(\Delta t_{i,\text{mea}} - \Delta t_{i,\text{calc}}\right)^2 \tag{1}$$

$$\Delta t_{i,\text{mea}} = t_i - t_1 \tag{2}$$

$$\Delta t_{i,\text{calc}} = \left[\sqrt{(X_i - X_s)^2 + (Y_i - Y_s)^2} - \sqrt{(X_1 - X_s)^2 + (Y_1 - Y_s)^2}\right] / v \tag{3}$$

where: X_k and Y_k are the coordinate, if the subscript is "S", it denotes the expected source position; otherwise, it means the location of the ith sensors; v is the wave propagation speed used in the calculations.

As each PBE test is repeated 3 times at the same location, the average coordinate and error in X and Y are shown in Table 1. It is noted that all errors in X coordinate are less than 1%, which is satisfied compared to exact PBE positions. On the contrary, the error in Y coordinate varies significantly from different AE sources. The relative position of PBE and predicted source location are illustrated in Fig. 7. The accurately predicted source positions in the middle section of the beam can be found in Fig. 7(b). In terms of the PBE locations near to upper and lower flanges, see Fig. 7(a) and (c), increasing errors are observed when the location of excitation moves towards the center of the beam. For instance, the PBE exerted at E7 is predicted at E9 (represented by the upward-

Table 1
The location results based TOA method.

PBE source location	X coordinate of the source (mm)	Predicted X coordinate (mm)	Error in X (%)	Y coordinate of the source (mm)	Predicted Y coordinate (mm)	Error in Y (%)
E1	1000	984	0.20	0	2.4e-5	0.006
E2	1000	1002	0.02	120	131	2.80
E3	1000	983	0.20	240	235	1.29
E4	2000	1981	0.23	0	14	3.62
E5	2000	1996	0.04	120	127	1.83
E6	2000	1977	0.28	240	192	12.1
E7	3000	3008	0.10	0	240	60
E8	3000	3030	0.36	120	174	13.5
E9	3000	3009	0.10	240	2.4e-5	60
E10	4000	4023	0.27	0	240	60
E11	4000	4003	0.03	120	165	11.3
E12	4000	4005	0.06	240	2.4e-5	60
E13	5000	5049	0.59	0	2.4e-5	0.006
E14	5000	5078	0.94	120	110	2.53
E15	5000	5082	0.99	240	240	0

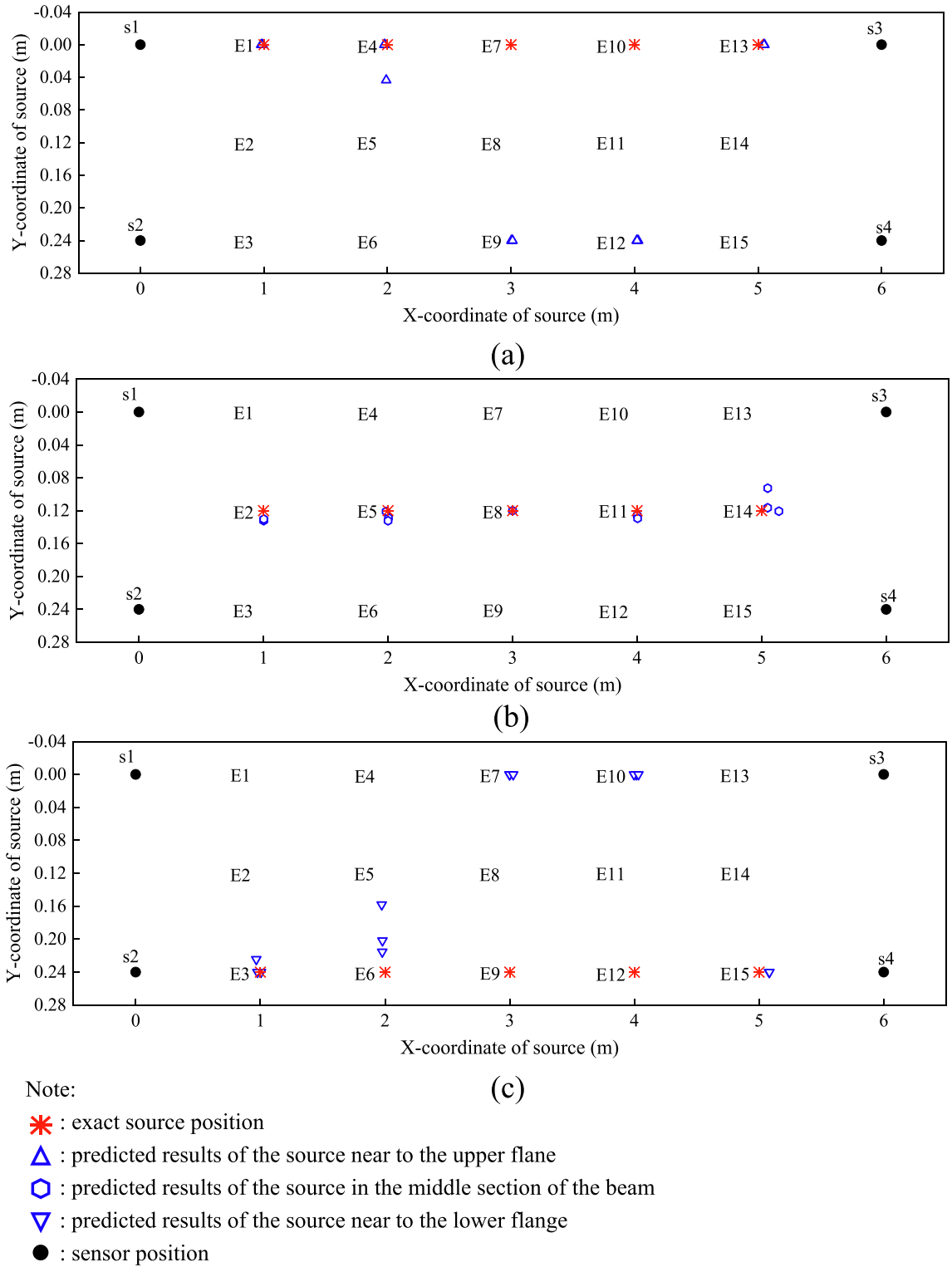

Fig. 7. Calculated source location results (a) near to the upper flange; (b) in the middle section of the beam and (c) near to the lower flange.

pointing triangle) in Fig. 7(a). It is approved that the accuracy of every source localization approach is limited by the experimental uncertainty of the system [41], including the experimental conditions, the acquisition system, and the changes in source position. However, the unneglectable errors around 60% of calculated source locations of E7, 9, 10, and 12 in Y coordinate cannot be explained by the uncertainty analysis of source localization accuracy.

3. Lamb wave propagation simulation

3.1. Numerical modeling

A FE model is created to perform a Lamb wave propagation within this complex structure using FE software ABAQUS, see Fig. 3. Generally, there are two effective ways to simulate Lamb

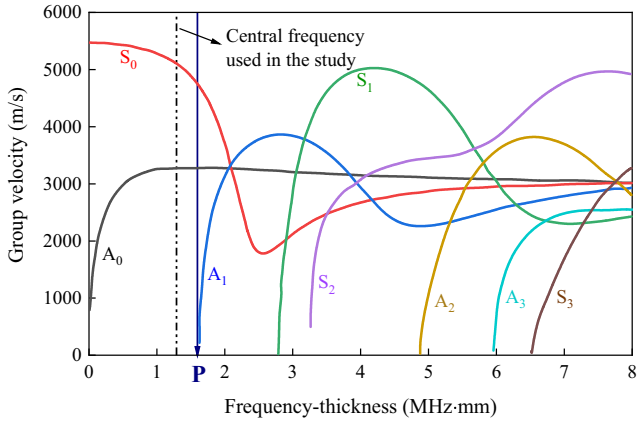

Fig. 8. Dispersion curves for Lamb waves in a steel plate [53].

wave propagation using the FE model in plate-like structures, which have been proven to be consistent with experimental results based on reported studies. For the first method, both the target structure and PZT transducers are modelled [14,49]. The disadvantages of this method are computationally expensive and time-consuming, which make it difficult to analyze complex and huge three-dimensional geometries. In the second method, no actual sensors are used to receive the wave signals [15,50]. The coupling effect between the PZT transducer and the target structure is therefore not needed in this method. Mesh nodes in the finite element model are used to mimic the excitation and sensor locations in corresponding experiments to save the computation time. The input can be equivalently represented by applying the out-of-plane force/displacement or uniform in-plane radial concentrated force. In this study, an out-of-plane in tone-burst in direction -X [51] (see Fig. 9) is used as the excitation, as Eq. (4), with the user-defined central frequency f_c and the number of cycles n_{cycle}.

$$y(t) = \sin(2\pi f_c t)\left[1 - \cos\left(\frac{2\pi f_c t}{n_{\text{cycle}}}\right)\right] \tag{4}$$

A predominate frequency of 150 kHz can be found after performing Fast Fourier Transform (FFT) of PBE signals obtained during experiments. Thus, a central frequency (f_c) of the excitation signal is selected as 150 kHz for the FE analysis of the wave propagation.

Lamb waves consist of two basic wave modes: symmetric modes (S_n) and anti-symmetric modes (A_n) due to its dispersive and multi-modal properties. Fig. 8 shows the relationship between group velocity and the product of plate thickness and the central frequency of Lamb waves [52]. Multiple Lamb wave modes can exist simultaneously when the frequency-thickness exceeds the critical value (Point P at Fig. 8). In this study, only the fundamental symmetric mode (S_0) and anti-symmetric mode (A_0) appears under a cut-off product with a value 1.29 MHz-mm (with the central frequency of 150 kHz and the web thickness of 8.6 mm), as the dash-dot line shown in Fig. 8. The TOA can be determined as the arrival time of the first received S_0/A_0 mode without the presence of higher-order Lamb mode ($n > 0$). The group velocity of S_0 mode and A_0 mode remains constant approximately as 5122 m/s and 3125 m/s, respectively.

The influence of cycle number was demonstrated by Kessler et al. [54] stating that the narrower band-width and less dispersive waves would be generated with increasing tone burst cycles. An excitation with more cycles could produce signals with longer duration resulting in overlapping between the propagating and scattering wave packets [55] and increasing difficulties of damage identification. To achieve an acceptable balance between bandwidth and duration, as shown in Fig. 9, a 3.5 cycle tone burst Hanning Window with a center frequency f_c of 150 kHz and amplitude value of 1 in terms of a larger ratio between the span and height is employed in this paper.

Numerical dispersion errors may occur when the FE model is applied to time-harmonic wave propagation problems due to spatial and time discretization. Previous studies have reported that the dispersion error could be reduced by using the time increments close to the stability limit and a finer mesh [56]. In order to ensure sufficient temporal and spatial resolution, the mesh size is recommended to be 1/10 wavelength [50]. Considering the numerical accuracy and computational efficiency, the entire geometry is meshed using different element size as 4 mm and 10 mm for steel girder and other parts, respectively. In total, the FEM model consisted of 4.3 million linear C3D8R hexahedral elements. The time increment is defined smaller than the critical values calculated from Eqs. (5) and (6) [57,58]. In this study, the time increment is set as 0.1 μs to make FE-generated signals consistent with the experimental facilities. Signals with a duration of 3000 μs are recorded during simulations.

$$\Delta t < 1/(20 f_{\max}) = 1/(20 \times 150\,\text{kHz}) = 0.333\,\mu s \tag{5}$$

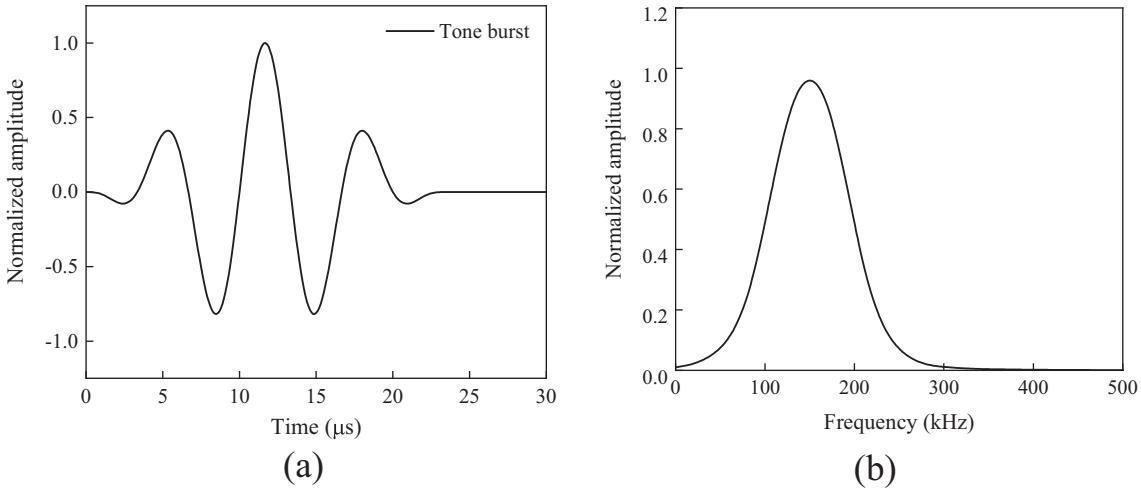

Fig. 9. The waveform used to generate signals: (a) time-domain and (b) frequency domain.

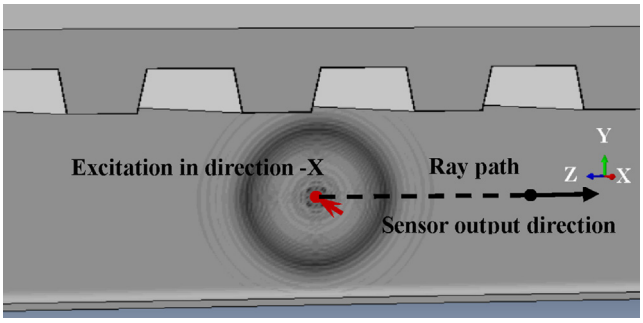

Fig. 10. Illustration of Lamb waves propagation in ABAQUS.

$$\Delta t < L_{\min}/c = 4\,\text{mm}/5122\,\text{m/s} = 0.791\,\mu s \tag{6}$$

where $f_{\max}$ is the central frequency of Lamb waves; $L_{\min}$ is the minimum element size; and c is the fastest wave speed, which can be obtained from the dispersive curves of Lamb wave as shown in Fig. 8.

3.2. Experimental verification in the linear array

To verify the reliability of the FE model, the numerical results under E1 to E7 in Fig. 5(a) are firstly compared to the experimental results. The Lamb waves propagate in a circular-crested pattern within the girder as shown in Fig. 10. The displacement of sensor nodes is extracted in the direction along the ray path between excitation and sensor nodes. The sensing voltage received by sensor 3 from both the FE simulation and the experiment is graphically illustrated in Fig. 11. The results show that extensional wave mode (S_0) propagates faster than flexural wave mode (A_0) and the amplitude of S_0 mode is lower than A_0 mode (a small amplitude precursor to the large flexural wave). When we observe two waveforms from the view of wave packets, these two waveforms show a reasonably good agreement. It is noted that the first received wave packet based on the FE simulation is earlier than the experimental result due to a perfectly smooth surface assumption in FE analysis. A minor variation in amplitude is observed in some packets. This is likely to be caused by the imperfections in the actual test specimen, such as surface roughness, geometrical imperfection, and position of PZT sensors. These imperfections could result in higher energy loss compared to the perfect FE model. Moreover, the displacement of a node is used for the analysis rather than an actual piezoelectric sensor in numerical modelling.

The arrival time and wave velocity are two key information required to be extracted from numerical results for source localization. Grosse [59] concluded that a typical PZT-sensor transforms elastic motions of 1 picometer (pm) displacement into electrical signals of 1 μV voltage. The relationship between voltage–time curves obtained from AEwin acquisition system and displacement–time curves acquired from the FE model can be established by normalization regarding the maximum amplitude. Similar to the threshold of voltage, the displacement threshold d_{thre} can be obtained acc. to Eq. (7):

$$d_{\text{thre}} = v_{\text{thre}}(d_{\max}/v_{\max}) \tag{7}$$

where v_{thre} means the threshold voltage set in AEwin system; $d_{\max}$ and $v_{\max}$ are the maximum value of displacement from numerical results and voltage from experimental results, respectively.

An example of the FE signals generated at E1 and obtained by sensors 5 and 6 is depicted in Fig. 12. Numerical results can record the complete information about the wave propagation instead of a limited waveform length from AEwin system. In that case, the wave velocity can be computed based on the time difference of arrival (TDOA) and the time of arrival (TOA). The average velocities using TDOA and TOA are 5240 m/s and 5266 m/s respectively, which are comparable with the experimental results 5219 m/s. It can thus be concluded that the simulated model is a suitable representation of the experiment.

3.3. Discussion about AE source location in the rectangular array

With the accuracy of the FE model verified in Section 3.2, the reason for ineffective source location in the rectangular array using the TOA method can be figured out in conjunction with the Lamb wave propagation simulation (Fig. 13). Numerical simulation of Lamb wave propagation is performed under the tone-burst excitation applied at E1 ~ E15 of Fig. 5(b). The Lamb wave packet induced by the tone burst at the FE model is shown in Fig. 13(a). Taking the excitation at E9 of the rectangular array (Fig. 13(d)) as an example, sensor 2 or 4 are supposed to receive the arrived wave at first. However, the wave arrives at sensor 1 firstly based on the experimental and numerical results, which is different from the results under the assumption of constant velocity. The accurate TOA and wave propagation velocity in different directions are calculated using the threshold displacement (d_{thre}). The velocities from E9 to sensor 1 and sensor 2 are 5106 m/s and 5023 m/s, respectively. The calculated velocity difference indicates that the sequence of signals arriving is affected significantly by reflection. The reflection caused by the lower flange has a stronger influence on the propagation than the top flange because the position of the exciter is clo-

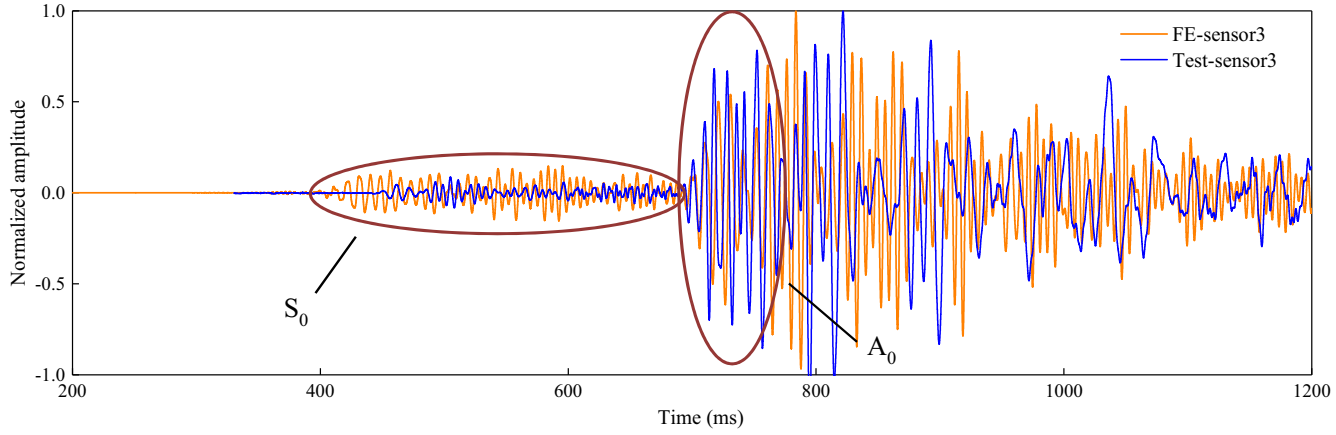

Fig. 11. Experimental vs. numerical signal received at sensor 3 under E1 of Fig. 5(a).

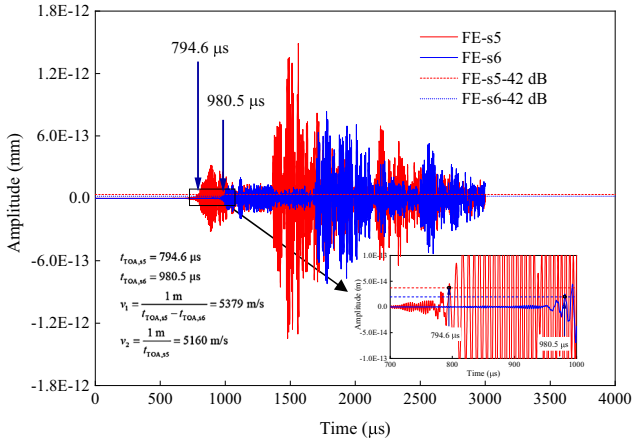

Fig. 12. Response signal and threshold line at sensor 5 (red) and sensor 6 (blue), from the FE model under E1 of Fig. 4(a). (For interpretation of the references to color in this figure legend, the reader is referred to the web version of this article.)

ser to the bottom flange. In conclusion, the boundary reflection has a strong influence on the scattering of the wave propagation path before the signals reach sensors [60]. The geometrical relationship between source and sensor also needs to be considered. Therefore, the assumption of constant velocity is certainly not suitable for source location in the I-girder. It can be concluded that the classical TOA method could not make a reliable interpretation of the data about acoustic emission signals.

4. TOA determination

4.1. Onset time detection methods

Accurate determination of the first arrival time of a signal is important to the accuracy of the source location. As mentioned before, the precision of onset time detection is easily influenced by reflections or scattered waves caused by irregular boundaries. TOA determined by the general user-defined threshold method is strongly dependent on the choice of the selected threshold value. Early triggering or missing true arrival time could occur with an arbitrarily set threshold value. Over the past few decades, various AE signal processing methods have been proposed for automatic detection of TOA, such as the Hinkley criterion, cumulative energy, power curve, and CWT-based binary map method. The following sections will discuss the TOA determination methods used in this paper.

4.1.1. Hinkley criterion

Grosse [59] developed a statistical method for onset time detection of AE signals based on the Hinkley criterion [61], as expressed in Eq. (8):

$$S_i' = S_i - i \cdot \delta = \sum_{k=0}^{i} R_k^2 - i \cdot \delta = \sum_{k=0}^{i} R_k^2 - i \cdot \frac{S_N}{\alpha \cdot N} \quad (i = 1 \text{ to } N)$$

where S'_i represents the modified partial energy with the introduction of a negative trend δ, so that the global minimum of S'_i is represented as the onset time; S_i is the partial energy calculated by the cumulative sum of i samples; R_k is the amplitude of k_{th} sample within the sample number i; S_N is the sum of the total energy of the signal with length N. The factor α is introduced to reduce a systematic delay of the global minimum with adding the negative trend. It is noted that the parameter α influences the results a lot (Fig. 14). The chosen value of α can be obtained by trial and error tests.

4.1.2. Cumulative energy

Bennoch and Judd [62] developed an approach which is based on the use of cumulative energy to determine the TOA of ultra-high frequency (UHF) signals. The voltage waveform is converted into a cumulative energy curve. The transit point is representative

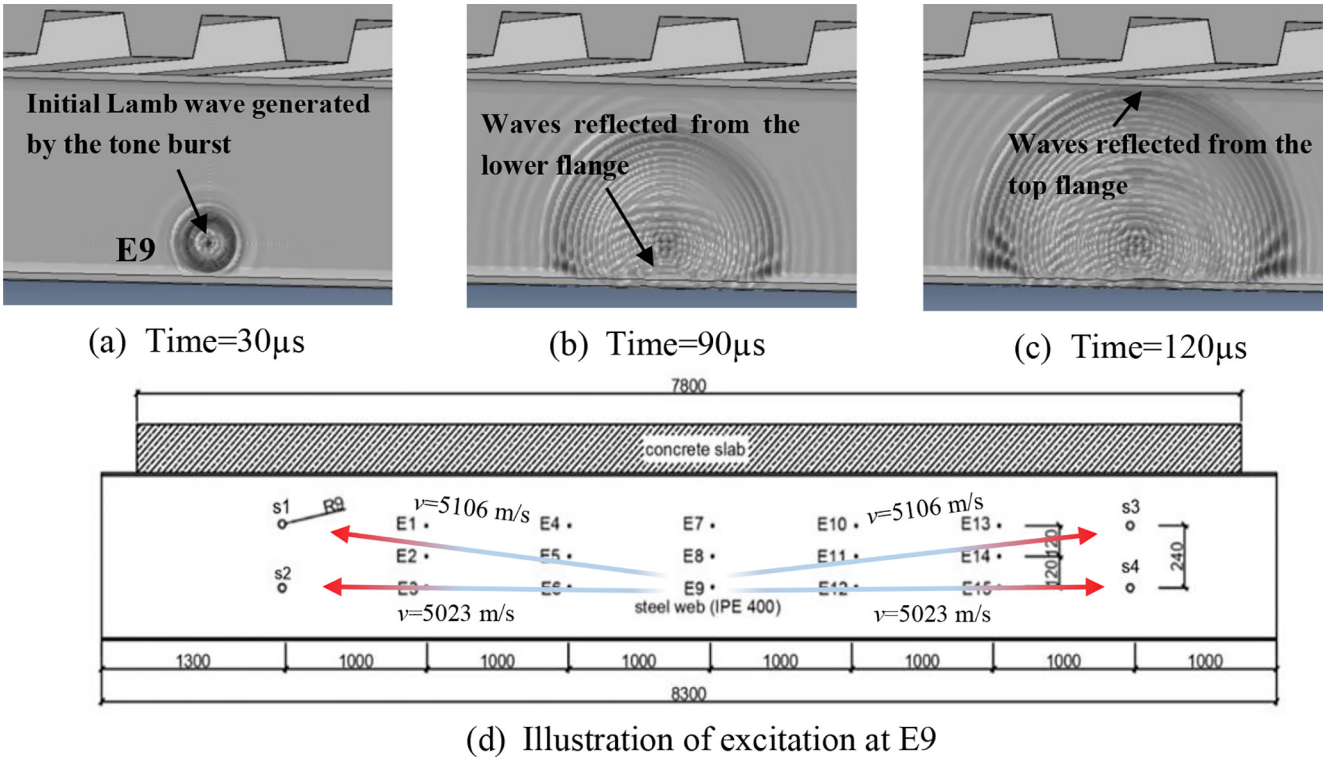

Fig. 13. Simulation of Lamb wave propagation in the girder.

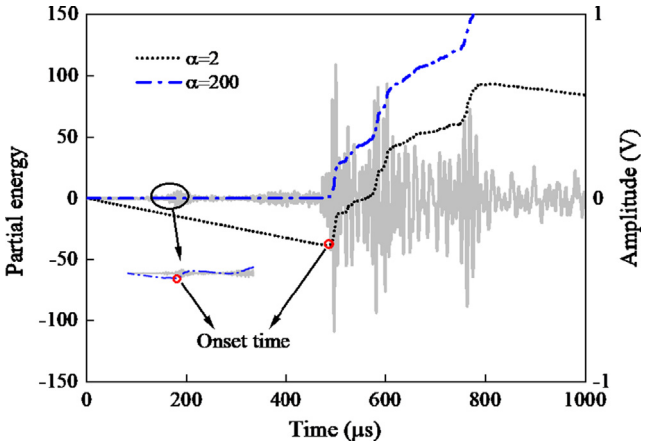

Fig. 14. Original signal and partial energy trend with different α.

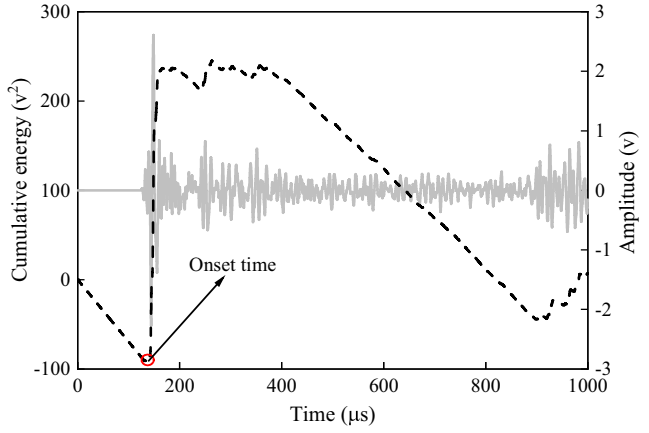

Fig. 15. Original signal and cumulative energy curve.

of the signal onset time (Fig. 15). A negative part was added to make the changeover point more apparent:

$$E_{neg}(n) = E_c(n) - n\frac{E_n}{N} = \sum_{m=0}^{n}\left(s^2(m) - n\frac{E_n}{N}\right) \quad (9)$$

where $E_c(n)$ is the cumulative energy of n samples using the voltage waveform $s(m)$; E_n is the total energy of the signal with the length of N.

4.1.3. Power curve

A simplified method using the power of voltage v_k^2 was proposed by Yang et. al [63]. Generally, the curve is normalized and a user-defined threshold is selected to pick the point whose amplitude is above the threshold. The determination of the threshold value is based on the signal–noise ratio of the detected signals. The threshold is suggested as 5% in most cases. If the signal is noisy, it is supposed to be set as 10% or more (Fig. 16).

4.1.4. Continuous wavelet transform-based binary map

Bai et. al [64] utilized Continuous wavelet transform (CWT) coefficients of a signal's time–frequency response to obtain a greyscale image. A nonlinear digital filtering technique called Median filter is then applied to minimize the presence of noise in the image. The onset time detection is performed automatically using Ostu's method by transforming the greyscale image to a binary map. The leading edge of the binary map can be identified as the onset time (Fig. 17). It should be noted that the leftmost non-zero pixel of the binary map is less obvious within heterogeneous materials or complex structures.

4.2. TOA results

The PBE signals received at sensor 1 and sensor 2 under E1 of the linear array (Fig. 5(a)) is illustrated in the examples. The Short-time Fourier transform (STFT) is calculated to generate a time–frequency representation of signals. The parameters corresponding to different methods are shown in Table 2. Figs. 18 and 19 show the distribution of TOA of the signals obtained from experimental results and FE simulation, respectively. The line in different colours indicates the detected TOA using various methods. The symmetric mode (S_0) and anti-symmetric mode (A_0) are clearly detected in Figs. 18(c)-(d) and 19(c)-(d). Generally, the S_0 and A_0 are generated at the same time and separate gradually due to their velocity difference [65]. As the position of sensor 1 is in close approximation to the excitation, the separation between these wave modes is not visible. Then, a noticeable separation can be observed of the signal at sensor 2 with sufficient source-to-sensor distance.

The relationship between TOA and source-to-sensor distance based on the experimental and FE results of the signals excited

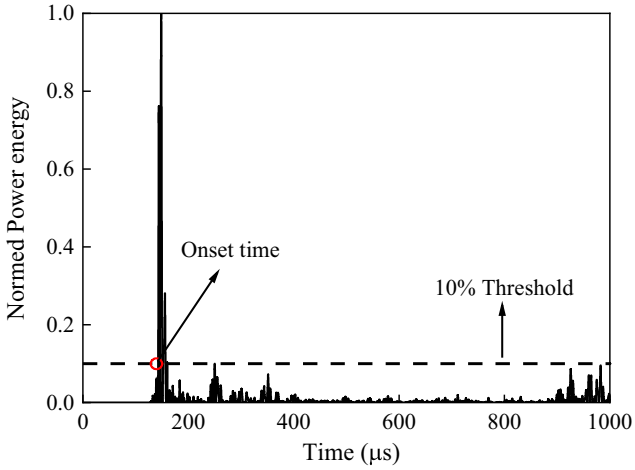

Fig. 16. Power energy curve.

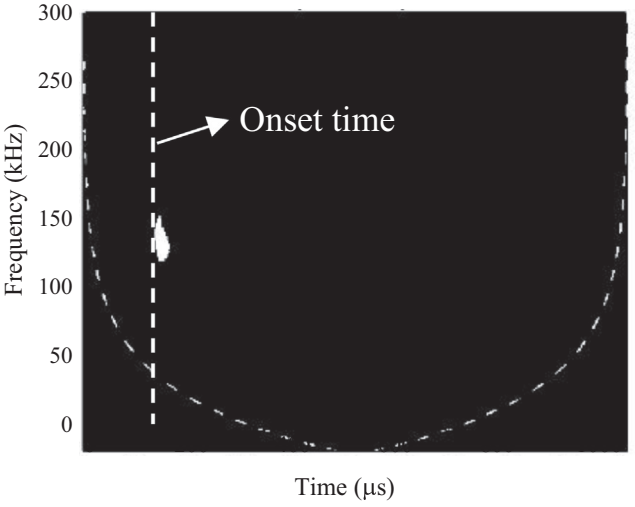

Fig. 17. AE signal onset time detection using CWT-based binary map.

Table 2
Results of onset time detection methods.

Method	Parameter	Value	Velocity-test (m/s)	Velocity-FE (m/s)
Threshold	Threshold level	12.6mV (42dB)	5219	5203
Hinkely Criterion	α	160	5202	5210
Cumulative Energy	–	–	3214	2993
Power curve	Threshold level	10%	3264	3000
CWT-based binary map	Mother wavelet	Morse	3202	2996

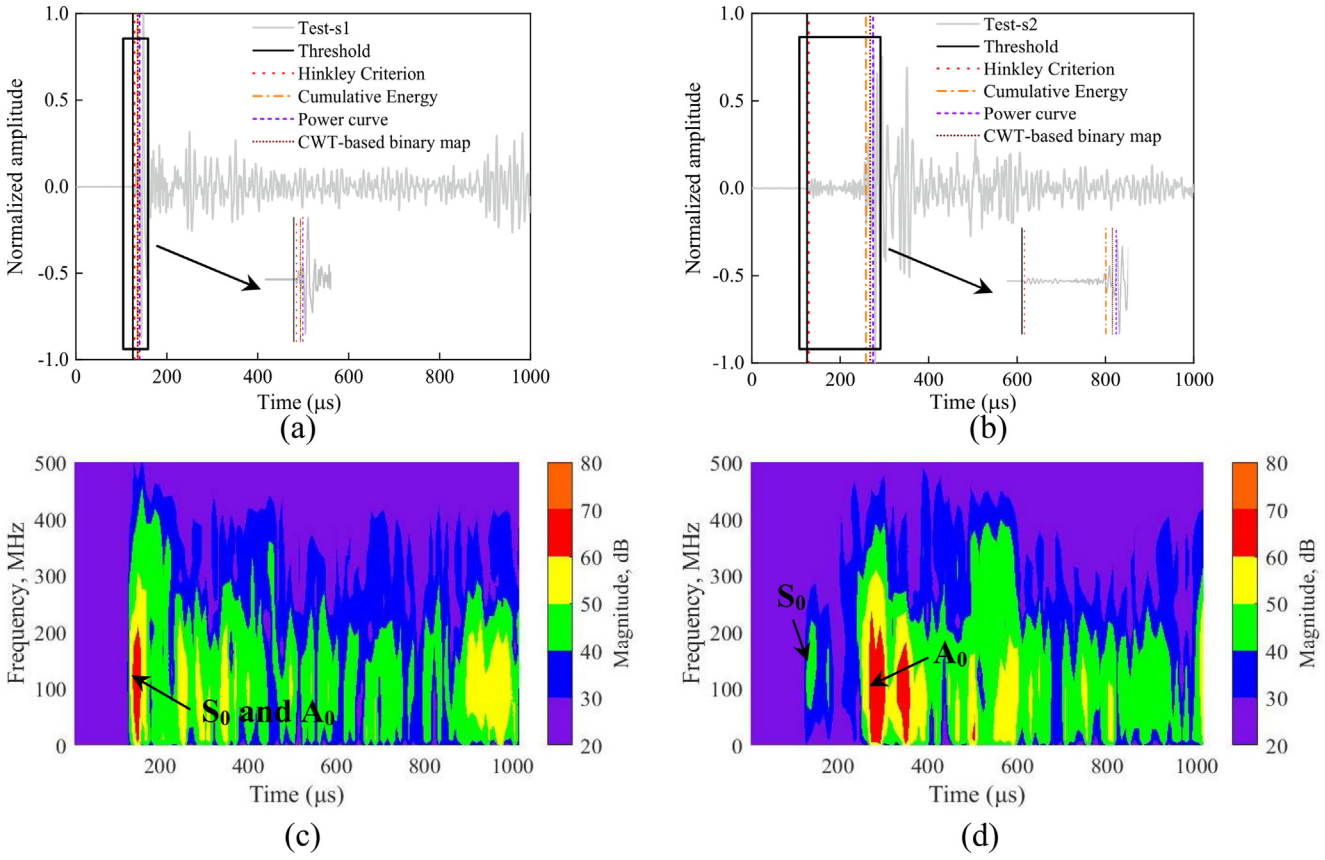

Fig. 18. Onset time detection of the signals obtained from experimental results: signals at (a) sensor 1 and (b) sensor 2; Amplitude spectrogram of signals at (c) sensor 1 and (d) sensor 2.

at E1 in Fig. 5(a) is depicted in Fig. 20. Wave propagation velocities related to each onset detection method are calculated by the ratio of source-to-sensor distance to TOA, as listed in Table 2. According to the wave dispersion curves of steel [52], the theoretical velocities of the S_0 mode and A_0 mode at 150 kHz are around 5000 m/s and 3000 m/s, respectively. In comparison to the theoretical velocities of wave modes, these onset detection methods can be categorized into two groups as shown in Table 3.

The Hinkley criterion is recommended because of its ability to detect onset times of S_0 wave mode [66,67]. Fig. 21 shows examples of comparison results of TDOA using the Hinkley criterion between the PBE tests and the simulation of the rectangular array. This good agreement demonstrates the reliability of the FE model and this onset time detection method further.

5. ANN-based source localization method

5.1. ANN development and training

The architecture of the network depends mainly on the available amount of data, which is established by simulation of the verified FE model to replace the need for a large number of experiments. A similar rectangular area to the experiments of Fig. 5(b) is used as the coordinate system of the source location. Fig. 22 illustrates the position of the tested area relative to the steel beam. Each acoustic signal is excited at 171 junction points produced by 9 × 19 grid lines. Additionally, five types of sensor layouts with 14 sensors are designed to find the influence of sensor arrangement on source location accuracy, as shown in Fig. 22 and Table 4. To ensure consistency and comparability between the TOA method and ANN-based method, the TDOA determined by Hinkley criterion method is used as the input database of ANN. It is noted that not all pair-wise combinations of sensors are used for source location, e.g. the case of four sensors creates three sensor pairs 1–2, 1–3, 1–4.

In this study, a multilayer feedforward ANN under supervision of an error-backpropagation (BP) algorithm is used for training. As shown in Fig. 23, the network consists of one input layer with an $(n\text{-}1) \times m$ matrix of TDOA symbolizing a total of m AE sources and n sensors, two hidden processing layers and two output layers with a $2 \times m$ matrix of the X and Y coordinate of m AE sources. In order to avoid under-fitting and over-fitting, the hidden layers

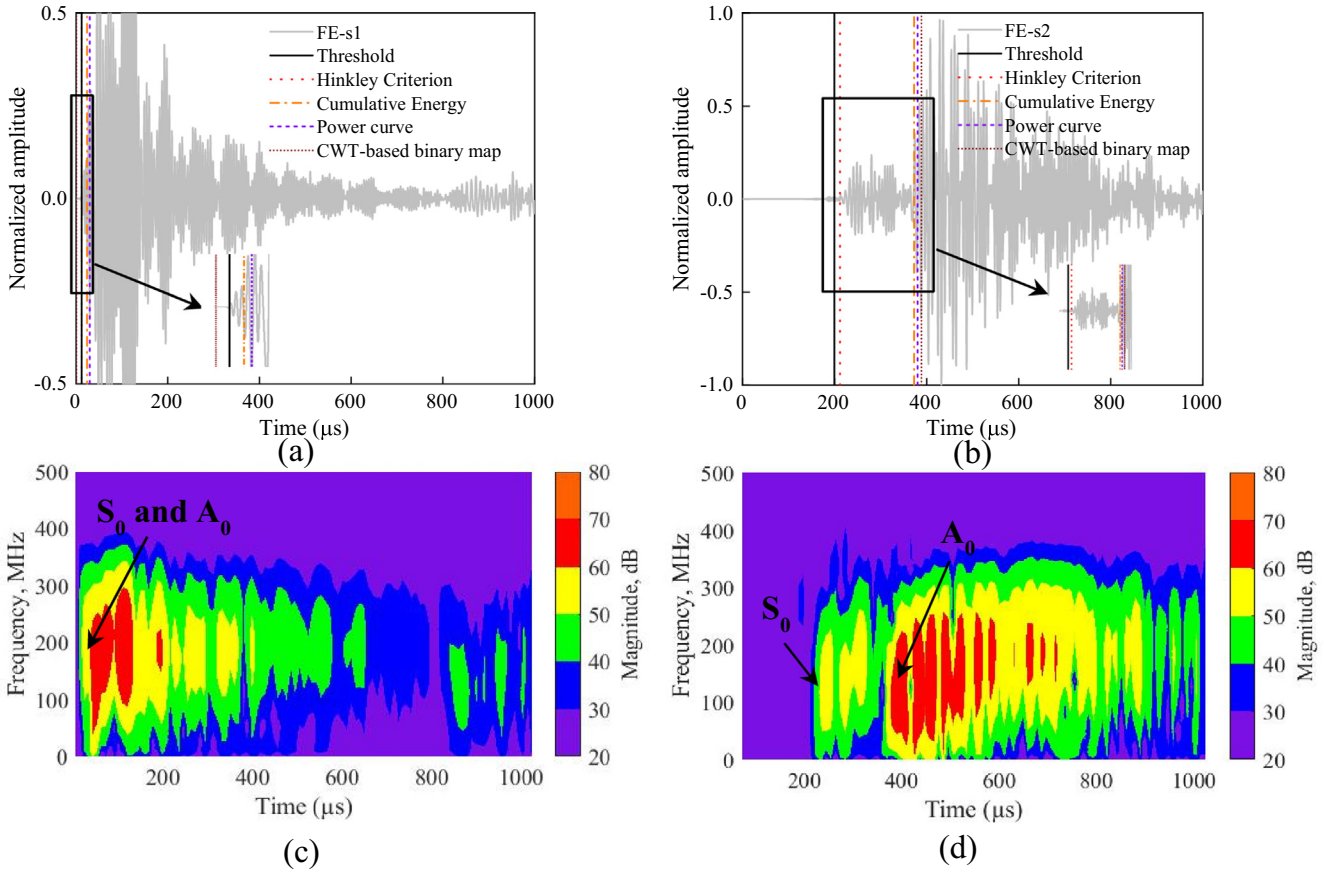

Fig. 19. Onset time detection of the signals obtained from FE simulation: signals at (a) sensor 1 and (b) sensor 2; Amplitude spectrogram of signals at (c) sensor 1 and (d) sensor 2.

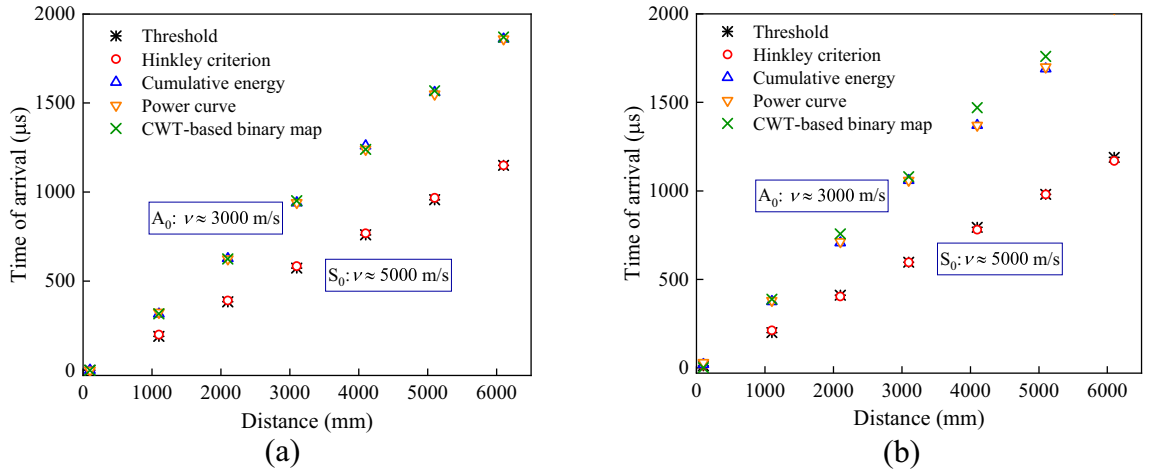

Fig. 20. TOA versus source-to-sensor distance curves of the signal source at E1 in the linear array: (a) Test results; (b) FE simulation.

Table 3
The classification of onset detection methods.

Methods for detecting S_0 modes	Methods for detecting A_0 modes
Hinkley Criterion	Cumulative Energy Power curve CWT-based binary map

with 20 (U_1) × 10 (U_2) neurons are chosen. The input dataset is usually randomly subdivided into the training set, validation set and test set with default ratios. A tip to improve the quality of the neural network and avoid overfitting is using specific indices to divide the dataset. The basic dataset (171 AE sources) is divided into 151 training points, 10 validation points and 10 test points. The performance of the model can be evaluated on the basis of

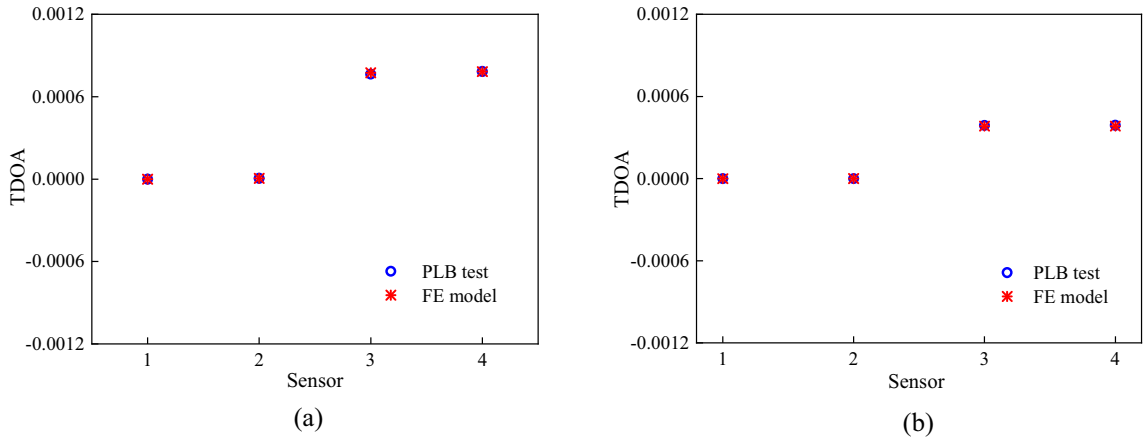

Fig. 21. Compsriaon of TDOA determined using Hinkely criterion between PBE tests and FE simulation: (a) Excitation at E1; (B) Excitation at E5 in Fig. 5(b).

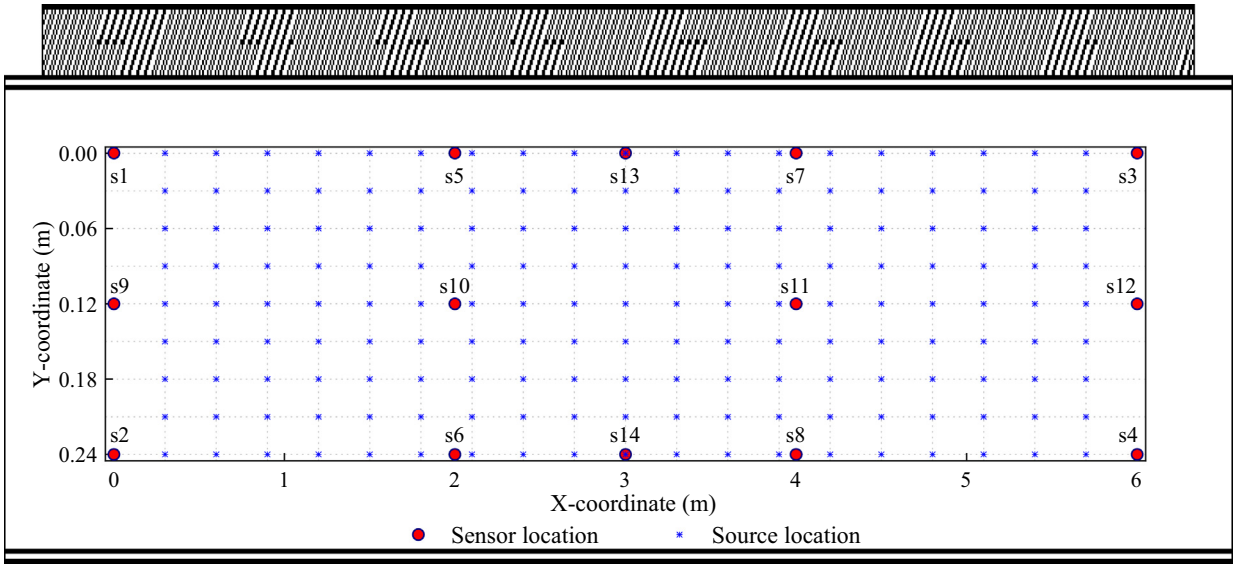

Fig. 22. Layout of sensors and excitations in the steel beam.

Table 4
The combination of sensors layout.

Case	Number of sensors	Combination
1	4	s1-s4
2	6	s1-s4 + s13-s14
3	8	s1-s8
4	10	s1-s8 + s9,s12
5	12	s1-s12

the R^2 (root-mean-square error (RMSE)) and the average deviation of the predicted output data to the known targets.

5.2. Comparison between TOA- and ANN-based source localization method

The source localization is carried out using the TOA method under Case1 at first. The source location quality using the classical TOA method along X and Y coordinate is displayed in Fig. 24(a) and (b) respectively. The spatial deviation between the position of excitation and the predicted position is represented by the color range in the image. Although only 171 excitations are analyzed, the error color map is acquired through thin-plate spline interpolation between the measurement with a smoothing parameter of 0.01. The color range is set from 0 to 15 cm to denote source localization error.

From Fig. 24(a) and (b), the localized Hsu-Nielsen source positions have an average deviation of 0.03 ± 3.3 cm in X coordinate and 0.06 ± 13.5 cm in Y coordinate. Considering the length of 8.3 m and height of 0.4 m of the I-shaped girder, the errors in X coordinate is considered acceptable as the maximum error is 10.8 cm (1.3% of the length of the girder). On the contrary, there is a larger deviation in the Y coordinate close to the flange at the center of the beam as shown in Fig. 22(b). The maximum error of 0.24 m is equivalent to 60% of the height of the girder, which is identical to the experimental results illustrated in Section 2.

For the same input data, the source location results using the neural network are shown in Fig. 24(c) and (d) with the same configurations under Case1. The range of error colour bar is selected to be identical. The maximum error in X coordinate decreases significantly from 10 cm with the TOA method to 2 cm with the ANN-base method. Additionally, the accuracy of the calculated Y coordinate is improved considerably with the mean source localization error of 0.06 ± 3.1 cm.

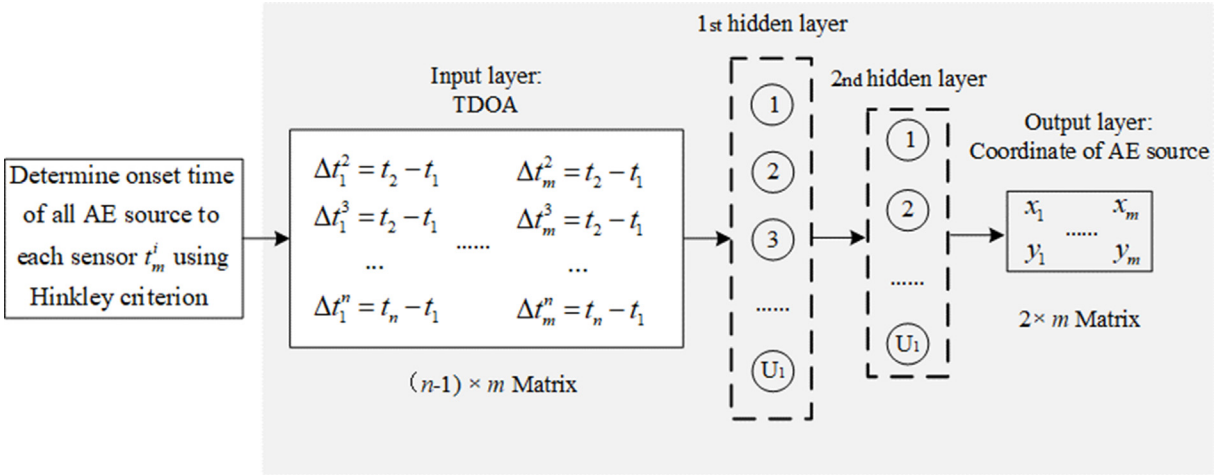

Fig. 23. Source localization method based on ANN.

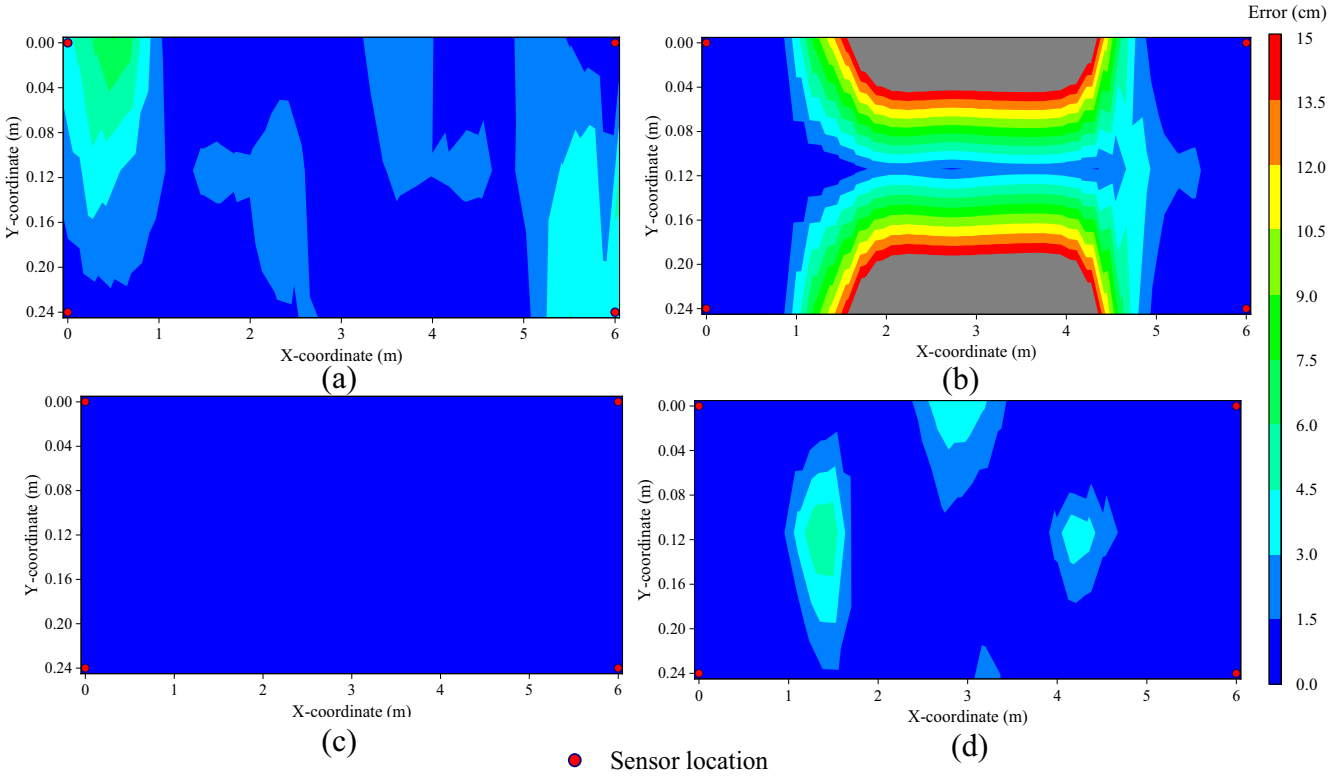

Fig. 24. Error color map of source localization in centimeters: Errors (a) in X coordinate using the TOA method; (b) in Y coordinate using the TOA method; (c) in X coordinate using ANN-based method; (d) in Y coordinate using ANN-based method.

5.3. Sensor arrangement

Considering the acceptable accuracy of source location in X coordinate, only the predicted source location results in Y coordinate under different cases are discussed. Fig. 25 depicts the comparison of error distribution in Y coordinate between the TOA method and ANN-based method. The error in Y coordinate is calculated as the ratio of error to the width of the girder. The results show that the improvement of the accuracy of predicting source location is achieved with the increasing number of sensors. However, the efficiency of improvement is small when the number of sensors is larger than 8 (from Case3 to Case5).

The detailed information of error distribution is shown in Fig. 26. From Fig. 26(a), even around 70% dataset obtained using the TOA method has an error of less than 10% in Case5, the largest error is up to 50%. Among the dataset using ANN-based method, more than 80% for Case1, 82% for Case2, 90% for Case3, 95% for Case4 and 99% for Case5 has an error within 10% as seen in Fig. 26(b), and the largest error is 22%, 14%, 15%, 16% 13% for Case1-5 respectively. The results show that the TOA method is less accurate than the ANN-based method under all investigated cases. ANN-based method offers significant improvements in the range of 21% to 41% on source localization accuracy. The effects including dispersion and boundary reflection can be effectively improved in the neural-network-based method.

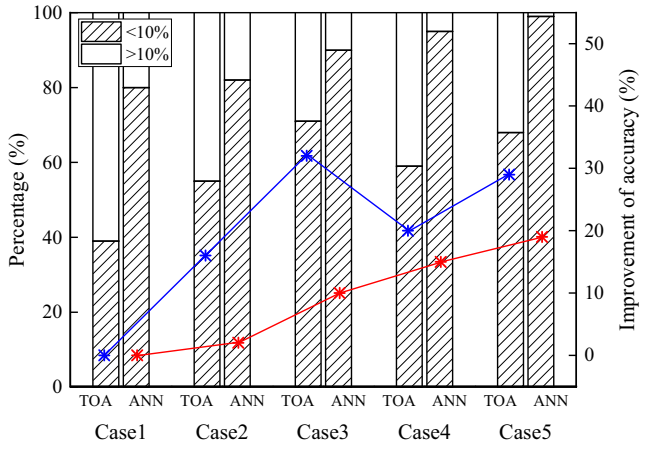

Fig. 25. Comparison of error distribution in Y coordinate between the TOA method and ANN-based method of all cases.

In addition, 12 virtual PBE tests (position is shown in Fig. 27(a)) are performed using FE analysis to obtain the input data for testing the trained networks. The error of outputs is used to quantify the reliability of the networks and the predicted results are illustrated in Fig. 27. In terms of Y coordinate, all trained networks can predict source location within the error limits of 10% from Fig. 27(b). The prediction accuracy is also dependent on the layout of the sensors. Based on the results showed in this paper, TOA method could not guarantee the prediction accuracy and ANN-based method could identify the damage (structural change/impact) even with a less number of sensors for the I-shape steel girder investigated in this paper.

6. Conclusions

The main objective of this study is to investigate an alternative and reliable localization method for global monitoring of life-size complex structures based on Artificial Neural Networks and Lamb Wave propagation simulation. Therefore, experimental and numerical analyses of an I-shaped composite steel–concrete girder are conducted. Based on the identical input data, a quantitative comparison of the ANN-based method and the TOA method is carried out. From the study, the following conclusions are drawn:

1. The feasibility of the TOA method for Hsu-Nielsen source location is identified in the tested I-girder. Although all the errors along the length direction of the girder are within 1%, the errors along height direction vary significantly from 0% to 60%. The possible sources of errors consist of the assumption of the constant velocity, TOA determined by user-defined threshold, and boundary reflection in the propagation path as shown by FE simulations.
2. The Lamb wave propagation induced from PBE is correctly simulated by the Finite Element Method using the excitation signal modulated as a 3.5 cycle tone burst with center frequency 150 kHz. A good agreement on the received signals, TOA determination, and the wave speed calculation is observed between PBE experiments and FE results. The FE model is proven to be a reliable alternative to the experiment.
3. Four onset time detection methods including the Hinkley criterion, cumulative energy, power curve, and CWT-based binary map method are discussed to overcome the limitation of the user-defined threshold method. The results show that different AE signal onset detection techniques correspond to different wave propagation modes, which is important to be considered for adequate damage type identification. Hinkley criterion is recommended as S_0 is more easily distinguishable than A_0.
4. The proposed ANN-based method could improve the accuracy of source localization significantly compared with the classical TOA method. The improvements of over 20% are seen in all cases with improvements up to 40% in some cases. All the trained networks can predict source location within the error limits of 10%. This proves the capability of using the ANN-based method to provide improved location prediction in the composite girder.

Although the presented method is validated by the specific steel–concrete composite girder, using the ANN-based method and numerical simulation for source location is expected to be reliable for source location in any real (composite) structures. The proposed method could also be used in the future for the design and optimization of the AE monitoring in realistic structures. Future

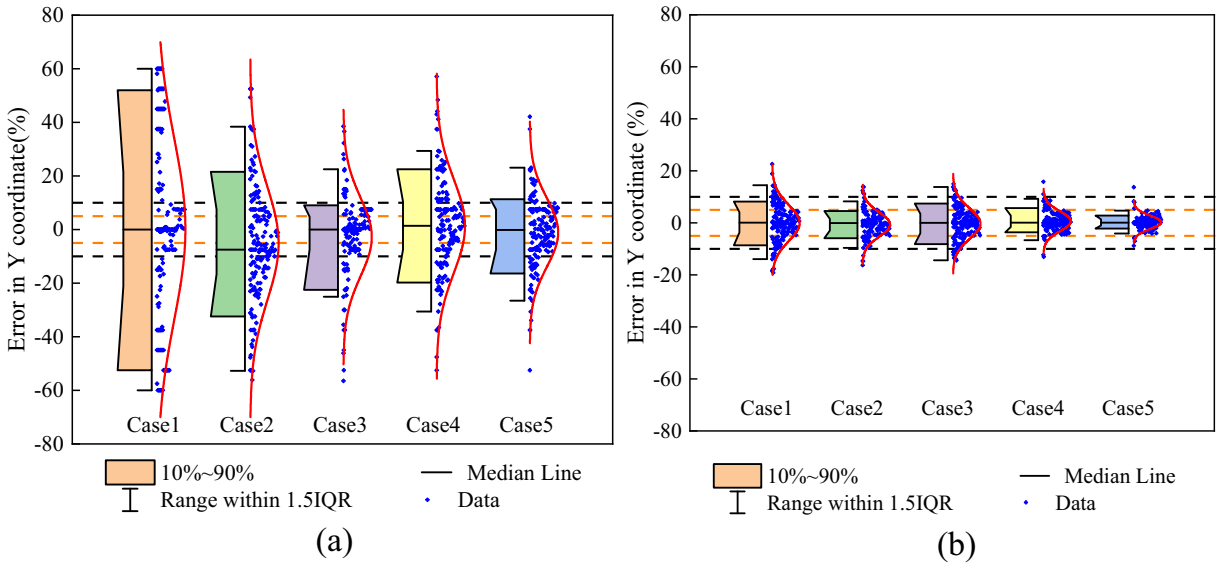

Fig. 26. Error distribution of all cases, limitation at ± 10% (black) and ± 5% (orange): (a) using the TOA method; (b) using ANN-based method. (For interpretation of the references to color in this figure legend, the reader is referred to the web version of this article.)

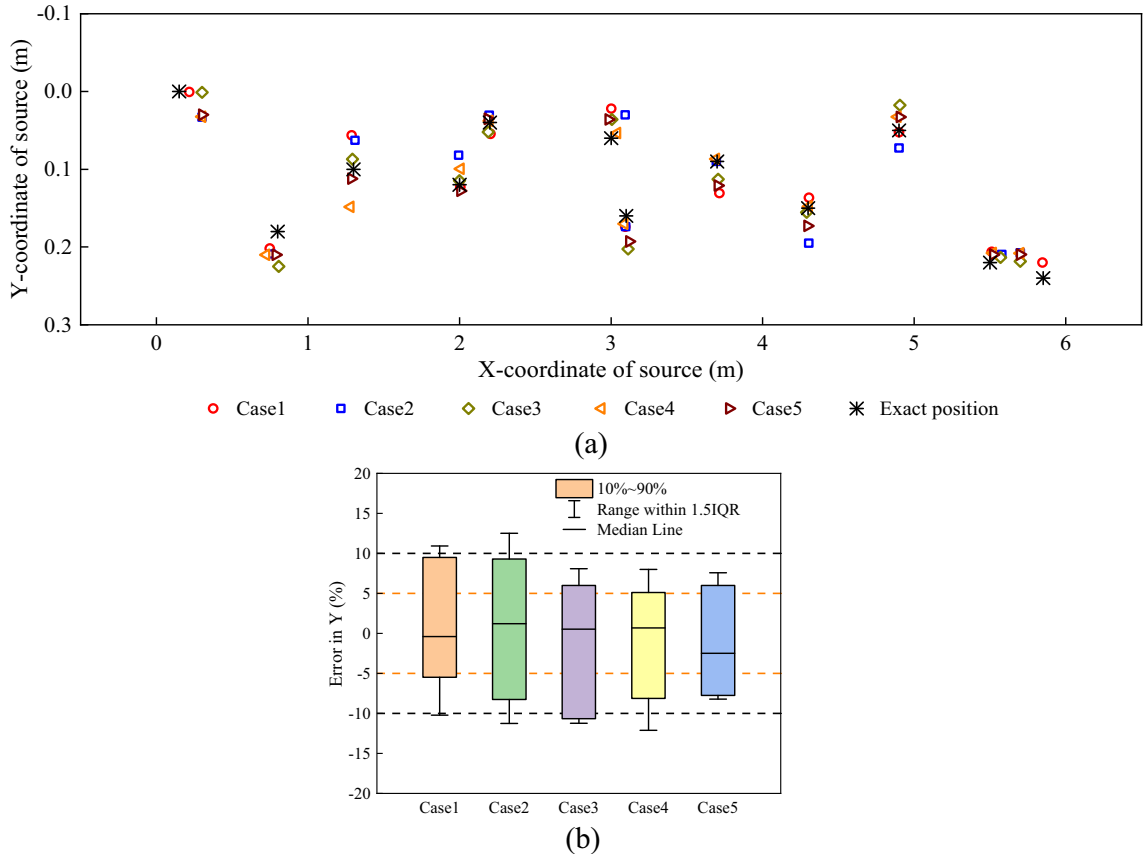

Fig. 27. Testing results of trained networks under all cases.

study is planned to focus on more quantitative AE analysis and in-depth investigations into three-dimensional source location of structures with complex geometry and actual damages.

CRediT authorship contribution statement

Lu Cheng: Formal analysis, Methodology, Investigation, Data curation, Writing - original draft. **Haohui Xin:** Conceptualization, Investigation, Writing - review & editing. **Roger M. Groves:** Writing - review & editing. **Milan Veljkovic:** Writing - review & editing.

Declaration of Competing Interest

The authors declare that they have no known competing financial interests or personal relationships that could have appeared to influence the work reported in this paper.

Acknowledgments

The first author wishes to express her gratitude for the financial support of the CSC Scholarship Council under grant number 201806060122.

References

[1] F. Ellyin, H. El-Kadi, A fatigue failure criterion for fiber reinforced composite laminae, Compos. Struct. 15 (1) (1990) 61–74.
[2] A.T. Green, C.S. Lockman, R.K. Steele, Acoustic verification of structural integrity of polaris chambers, Mod. Plast. 41 (11) (1964) 137–139.
[3] Q. Feng, Q. Kong, L. Huo, G. Song, Crack detection and leakage monitoring on reinforced concrete pipe, Smart Mater. Struct. 24 (11) (2015) 115020.
[4] H. Xin, L. Cheng, R. Diender, M. Veljkovic, Fracture acoustic emission signals identification of stay cables in bridge engineering application using deep transfer learning and wavelet analysis, Adv. Bridg. Eng. 1 (1) (2020) 1–16.
[5] K.M. Holford, A.W. Davies, R. Pullin, D.C. Carter, Damage location in steel bridges by acoustic emission, J. Intell. Mater. Syst. Struct. 12 (8) (2001) 567–576.
[6] M.G. Baxter, R. Pullin, K.M. Holford, S.L. Evans, Delta T source location for acoustic emission, Mech. Syst. Sig. Process. 21 (3) (2007) 1512–1520.
[7] I. Park, Y. Jun, U. Lee, Lamb wave mode decomposition for structural health monitoring, Wave Motion 51 (2) (2014) 335–347.
[8] Z. Wang, P. Qiao, B. Shi, Application of soft-thresholding on the decomposed Lamb wave signals for damage detection of plate-like structures, Measurement 88 (2016) 417–427.
[9] P. Kudela, M. Radzienski, W. Ostachowicz, Z. Yang, Structural Health Monitoring system based on a concept of Lamb wave focusing by the piezoelectric array, Mech. Syst. Sig. Process. 108 (2018) 21–32.
[10] M. Abbas, M. Shafiee, Structural health monitoring (SHM) and determination of surface defects in large metallic structures using ultrasonic guided waves, Sensors. 18 (11) (2018) 3958.
[11] J.L. Rose, A baseline and vision of ultrasonic guided wave inspection potential, J. Press. Vessel Technol. Trans. ASME. 124 (3) (2002) 273–282.
[12] M.A.A. Aldahdooh, N.M. Bunnori, M.A. Megat Johari, Damage evaluation of reinforced concrete beams with varying thickness using the acoustic emission technique, Constr. Build. Mater. 44 (2013) 812–821.
[13] C. Lee, S. Park, J.E. Bolander, S. Pyo, Monitoring the hardening process of ultra high performance concrete using decomposed modes of guided waves, Constr. Build. Mater. 163 (2018) 267–276.
[14] Z.S. Tang, Y.Y. Lim, S.T. Smith, I. Izadgoshasb, Development of analytical and numerical models for predicting the mechanical properties of structural adhesives under curing using the PZT-based wave propagation technique, Mech. Syst. Sig. Process. 128 (2019) 172–190.
[15] V. Ewald, R.M. Groves, R. Benedictus, Transducer Placement Option of Lamb Wave SHM System for Hotspot Damage Monitoring, Aerospace. 5 (2) (2018) 39.
[16] C.-T. Ng, H. Mohseni, H.-F. Lam, Debonding detection in CFRP-retrofitted reinforced concrete structures using nonlinear Rayleigh wave, Mech. Syst. Sig. Process. 125 (2019) 245–256.
[17] O. Yapar, P.K. Basu, P. Volgyesi, A. Ledeczi, Structural health monitoring of bridges with piezoelectric AE sensors, Eng. Fail. Anal. 56 (2015) 150–169.
[18] D. Li, K.S.C. Kuang, C.G. Koh, Fatigue crack sizing in rail steel using crack closure-induced acoustic emission waves, Meas. Sci. Technol. 28 (6) (2017) 065601.

[19] J. Yu, P. Ziehl, B. Zárate, J. Caicedo, Prediction of fatigue crack growth in steel bridge components using acoustic emission, J. Constr. Steel Res. 67 (8) (2011) 1254–1260.
[20] B.A. Zárate, J.M. Caicedo, J. Yu, P. Ziehl, Deterministic and probabilistic fatigue prognosis of cracked specimens using acoustic emissions, J. Constr. Steel Res. 76 (2012) 68–74.
[21] M. Rucka, Monitoring steel bolted joints during a monotonic tensile test using linear and nonlinear lamb wave methods: A feasibility study, Metals (Basel). 8 (9) (2018) 683.
[22] A. Karolczuk, J. Papuga, T. Palin-Luc, Progress in fatigue life calculation by implementing life-dependent material parameters in multiaxial fatigue criteria, Int. J. Fatigue 134 (2020) 105509.
[23] C.U. Grosse, M. Ohtsu, Acoustic Emission Testing, 2008.
[24] K.R. Miller, E.K. Hill, Non-destructive Testing Handbook, Acoustic Emission Testing, American S, 2005.
[25] A. Khalili, N. Jayakody, R. Jha, Structural Health Monitoring of Skin-Stiffener Structures Using WSFE-based User Defined Elements in Abaqus, in: 25th AIAA/AHS Adapt. Struct. Conf., 2017.
[26] Z.A.B. Ahmad, U. Gabbert, Simulation of Lamb wave reflections at plate edges using the semi-analytical finite element method, Ultrasonics 52 (7) (2012) 815–820.
[27] A. Nair, C.S. Cai, Acoustic emission monitoring of bridges: Review and case studies, Eng. Struct. 32 (6) (2010) 1704–1714.
[28] A. Mostafapour, S. Davoodi, M. Ghareaghaji, Acoustic emission source location in plates using wavelet analysis and cross time frequency spectrum, Ultrasonics 54 (8) (2014) 2055–2062.
[29] M. Koabaz, T. Hajzargarbashi, T. Kundu, M. Deschamps, Locating the acoustic source in an anisotropic plate, Struct. Health Monit. 11 (3) (2012) 315–323.
[30] A. Ebrahimkhanlou, S. Salamone, Acoustic emission source localization in thin metallic plates: a single-sensor approach based on multimodal edge reflections, Ultrasonics 78 (2017) 134–145.
[31] T. Kundu, X. Yang, H. Nakatani, N. Takeda, A two-step hybrid technique for accurately localizing acoustic source in anisotropic structures without knowing their material properties, Ultrasonics 56 (2015) 271–278.
[32] J. Tai, T. He, Q. Pan, D. Zhang, X. Wang, A fast beamforming method to localize an acoustic emission source under unknown wave speed, Materials (Basel). 12 (5) (2019) 735.
[33] B.A. Zárate, A. Pollock, S. Momeni, O. Ley, Structural health monitoring of liquid-filled tanks: a Bayesian approach for location of acoustic emission sources, Smart Mater. Struct. 24 (1) (2015) 015017.
[34] M.S. Hameed, Z. Li, J. Chen, J. Qi, Lamb-Wave-Based Multistage Damage Detection Method Using an Active PZT Sensor Network for Large Structures, Sensors (Basel). 19 (9) (2019) 2010.
[35] S.K. Al-Jumaili, M.R. Pearson, K.M. Holford, M.J. Eaton, R. Pullin, Acoustic emission source location in complex structures using full automatic delta T mapping technique, Mech. Syst. Sig. Process. 72-73 (2016) 513–524.
[36] M.R. Pearson, M. Eaton, C. Featherston, R. Pullin, K. Holford, Improved acoustic emission source location during fatigue and impact events in metallic and composite structures, Struct. Health Monit. 16 (4) (2017) 382–399.
[37] S. Farhangdoust, S. Tashakori, A. Baghalian, A. Mehrabi, I. N. Tansel, Prediction of damage location in composite plates using artificial neural network modeling, in: K.-W. Wang, H. Sohn, H. Huang, J.P. Lynch (Eds.), Sensors Smart Struct. Technol. Civil, Mech. Aerosp. Syst. 2019 Int. Soc. Opt. Photonics., SPIE, 2019.
[38] V. Soltangharaei, R. Anay, L. Assi, M. Bayat, J.R. Rose, P. Ziehl, Analyzing acoustic emission data to identify cracking modes in cement paste using an artificial neural network, Constr. Build. Mater. (2020) 121047.
[39] M.A. Pillai, A. Ghosh, J. Joy, S. Kamal, C.C. Satheesh, A.A. Balakrishnan, M.H. Supriya, Acoustic Source Localization using Random Forest Regressor, in: Int. Symp. Ocean Electron. SYMPOL, IEEE Computer Society, 2019: pp. 191–199.
[40] Z.H. Liu, Q.L. Peng, X. Li, C.F. He, B. Wu, Acoustic Emission Source Localization with Generalized Regression Neural Network Based on Time Difference Mapping Method, Exp. Mech. 60 (5) (2020) 679–694.
[41] S. Kalafat, M.G.R. Sause, Acoustic emission source localization by artificial neural networks, Struct. Health Monit. 14 (6) (2015) 633–647.
[42] A. De Fenza, A. Sorrentino, P. Vitiello, Application of artificial neural networks and probability ellipse methods for damage detection using Lamb waves, Compos. Struct. 133 (2015) 390–403.
[43] D.T Pham, P.T.N Pham, Artificial intelligence in engineering, Int. J. Mach. Tools Manuf. 39 (6) (1999) 937–949, https://doi.org/10.1016/S0890-6955(98)00076-5.
[44] Y.Y. Lim, K.Z. Kwong, W.Y.H. Liew, R.V. Padilla, C.K. Soh, Parametric study and modeling of PZT based wave propagation technique related to practical issues in monitoring of concrete curing, Constr. Build. Mater. 176 (2018) 519–530.
[45] P. Ochôa, R.M. Groves, R. Benedictus, Systematic multiparameter design methodology for an ultrasonic health monitoring system for full-scale composite aircraft primary structures, Struct. Control Health Monit. 26 (5) (2019) e2340.
[46] A.N. Ede, P.F. Adepoju, P.O. Awoyera, Challenges of car pack design in Nigeria, Int. J. Innov. Technol. Explor. Eng. 4 (10) (2015) 38–42.
[47] M.G.R. Sause, Investigation of pencil-lead breaks as acoustic emission sources, J. Acoust. Emiss. 29 (2011) 184–196.
[48] M.J. Eaton, R. Pullin, K.M. Holford, Towards improved damage location using acoustic emission, Proc. Inst. Mech. Eng., Part C 226 (9) (2012) 2141–2153.
[49] S. Sikdar, W. Ostachowicz, Ultrasonic Lamb wave-based debonding monitoring of advanced honeycomb sandwich composite structures, Strain 55 (1) (2019) e12302.
[50] J. He, Y. Ran, B. Liu, J. Yang, X. Guan, A fatigue crack size evaluation method based on lamb wave simulation and limited experimental data, Sensors. 17 (9) (2017) 2097.
[51] E. Palmos, Modeling of Lamb waves and application to crack identification, Naval Postgraduate School (2009).
[52] O. Diligent, T. Grahn, A. Boström, P. Cawley, M.J.S. Lowe, The low-frequency reflection and scattering of the S0 Lamb mode from a circular through-thickness hole in a plate: Finite Element, analytical and experimental studies, J. Acoust. Soc. Am. 112 (6) (2002) 2589–2601.
[53] A. Crawford, M.G. Droubi, N.H. Faisal, Analysis of acoustic emission propagation in metal-to-metal adhesively bonded joints, J. Nondestruct. Eval. 37 (2) (2018).
[54] S.S. Kessler, S.M. Spearing, C. Soutis, Damage detection in composite materials using Lamb wave methods, Smart Mater. Struct. 11 (2) (2002) 269–278.
[55] K. Sun, G. Meng, F. Li, L. Ye, Y. Lu, Damage identification in thick steel beam based on guided ultrasonic waves, J. Intell. Mater. Syst. Struct. 21 (3) (2010) 225–232.
[56] M.N. Guddati, B. Yue, Modified integration rules for reducing dispersion error in finite element methods, Comput. Methods Appl. Mech. Eng. 193 (3-5) (2004) 275–287.
[57] S. Han, A.N. Palazotto, C.L. Leakeas, Finite-element analysis of Lamb wave propagation in a thin aluminum plate, J. Aerosp. Eng. 22 (2) (2009) 185–197.
[58] F. Moser, L.J. Jacobs, J. Qu, Modeling elastic wave propagation in waveguides with the finite element method, NDT E Int. 32 (4) (1999) 225–234.
[59] C.U. Grosse, Winpecker version 1.2: instruction manual, Univ. Stuttgart. (2000).
[60] M. Gresil, V. Giurgiutiu, Prediction of attenuated guided waves propagation in carbon fiber composites using Rayleigh damping model, J. Intell. Mater. Syst. Struct. 26 (16) (2015) 2151–2169.
[61] D. V. Hinkley, Inference about the change-point from cumulative sum tests, Biometrika. 58 (3) (1971) 509–523.
[62] C. Bennoch, M. Judd, A UHF system for characterizing individual PD sources within a multi-source environment, in: 13th Int. Symp. High Volt. Eng., 2003.
[63] L. Yang, M.D. Judd, C.J. Bennoch, Time delay estimation for UHF signals in PD location of transformers, in: 17th Annu. Meet. IEEE Lasers Electro-Optics Soc., IEEE, 2004: pp. 414–417.
[64] F. Bai, D. Gagar, P. Foote, Y. Zhao, Comparison of alternatives to amplitude thresholding for onset detection of acoustic emission signals, Mech. Syst. Signal Process. 84 (2017) 717–730, https://doi.org/10.1016/j.ymssp.2016.09.004.
[65] D. Aljets, A. Chong, S. Wilcox, K. Holford, Acoustic emission source location in plate-like structures using a closely arranged triangular sensor array, J. Acoust. Emiss. 28 (2010) 85–98.
[66] H.L. Dunegan, Modal analysis of acoustic emission signals, J. Acoust. Emiss. 15 (1997) 53–61.
[67] M.R. Gorman, W.H. Prosser, AE source orientation by plate wave analysis, J. Acoust. Emiss. 9 (4) (1991) 283–288.